Translational Oncology

www.transonc.com

Volume 6 Number 3 June 2013 pp. 347–354 347

MRI Detection of Nonproliferative Tumor Cells in Lymph Node Metastases Using Iron Oxide Particles in a Mouse Model of Breast Cancer[1]

Vasiliki Economopoulos*,†, Yuhua Chen†, Catherine McFadden† and Paula J. Foster*,†

*Department of Medical Biophysics, Robarts Research Institute at the University of Western Ontario, London, Ontario, Canada; †Imaging Research Group, Robarts Research Institute at the University of Western Ontario, London, Ontario, Canada

Abstract

Cell tracking with magnetic resonance imaging (MRI) and iron nanoparticles is commonly used to monitor the fate of implanted cells in preclinical disease models. Few studies have employed these methods to study cancer cells because proliferative iron-labeled cancer cells will lose the label as they divide. In this study, we evaluate the potential for retention of the iron nanoparticle label, and resulting MRI signal, to serve as a marker for slowly dividing cancer cells. Green fluorescent protein–transfected MDA-MB-231 breast cancer cells were labeled with red fluorescent micron-sized superparamagnetic iron oxide (MPIO) nanoparticles. Cells were examined *in vitro* at multiple time points after labeling by staining for iron-labeled cells and by flow cytometric detection of the fluorescent MPIO. Severe combined immune deficiency (SCID) mice were implanted with 5×10^5 MPIO-labeled or unlabeled cells in the mammary fat pad and MRI was performed weekly until 28 days after injection. Microscopy was performed to validate MRI. *In vitro* assays revealed a very small percentage of cells that retained MPIO at 14 days after labeling. Regions of signal loss were observed in MRI of primary tumors that developed from iron-labeled cancer cells. Small focal regions of signal loss were detected in images of the axillary and brachial nodes in six of eight mice, at day 14 or later, with microscopy confirming the presence of iron-labeled cancer cells. Our data suggest an interesting role for cell tracking with iron particles since label retention leads to persistent signal void, allowing proliferative status to be determined.

Translational Oncology (2013) 6, 347–354

Introduction

Magnetic resonance imaging (MRI) is a commonly used imaging method for tracking cells *in vivo* in preclinical models of disease. To accomplish this, cells are labeled with a contrast agent before their injection or transplantation. Most cell tracking studies have used superparamagnetic iron oxide (SPIO) nanoparticles for cell labeling. SPIO particles disturb the static magnetic field, and this effect extends well beyond the volume of the cell, resulting in a dramatic reduction in the T2 and T2* of nearby water molecules. T2- and T2*-based imaging methods depict SPIO-labeled cells as pronounced local signal voids or hypointense regions [1]. A variety of cell types has been studied using this approach. Examples include monitoring the fate of transplanted stem/progenitor cells in myocardial infarction [2,3], stroke [4], spinal cord injury [5,6], and multiple sclerosis [7] and detecting the migration of dendritic cells used in cancer immunotherapy [8–10]. While most studies focus on the visualization of relatively large numbers of cells, even single iron-labeled cells can be detected *in vivo* by MRI [11,12].

Few groups have used iron nanoparticles and MRI to track cancer cells. This is primarily because the SPIO label is diluted over time in dividing cells leading to loss of signal and therefore loss of cell detection

Address all correspondence to: Paula J. Foster, PhD, Scientist and Associate Professor, Imaging Research Laboratories, Robarts Research Institute, University of Western Ontario, 100 Perth Drive, Rm 1200B, London, Ontario, Canada N6A 5K8.
E-mail: pfoster@robarts.ca

[1]We acknowledge the Canadian Cancer Society Research Institute for funding and the Canadian Breast Cancer Foundation, Ontario Region for salary support for V.E. through a doctoral fellowship.
Received 15 January 2013; Revised 7 February 2013; Accepted 8 February 2013

1944-7124/13 DOI 10.1593/tlo.13121

[13]. However, we and others have shown that the retention of iron particles in nonproliferative, or slowly cycling, cancer cells can be exploited to detect particular cancer cell populations [14–16]. Heyn et al. demonstrated that a small percentage of brain metastatic human breast cancer cells arrest in the mouse brain and persist as distinct signal voids in a nonproliferative state, while another population of cancer cells proliferate and form brain metastases [14]. Townson et al. injected iron-labeled metastatic melanoma cells into the mouse liver and used MRI to show that cytotoxic chemotherapy with doxorubicin reduced liver tumor burden but did not affect the number of nonproliferative cancer cells [15]. Iron-retaining cancer cells have also been observed by MRI in melanoma xenografts implanted subcutaneously in mice [16]; Magnitsky et al. demonstrated that a small, distinct subpopulation of iron-retaining cells could be detected by flow cytometry after 20 days of *in vitro* proliferation [16]. These papers all demonstrated the ability to use iron nanoparticles and MRI to image cells with a slow proliferation phenotype.

The cells these papers are targeting have been referred to as nonproliferative, quiescent, slowly cycling, or dormant. Despite the diverse nomenclature, the common goal of these studies has been to characterize a subpopulation of cancer cells that is believed to play a critical role in tumor progression and metastasis. Several experimental metastasis models, using a variety of cancer cell lines, show the presence of nonproliferative cancer cells, often coexisting in a metastatic site with actively growing metastases [17–19]. In breast cancer, metastatic cancer cells can sometimes remain dormant for decades until some poorly understood trigger causes them to proliferate and progress to clinically relevant metastases [20].

In this paper, we use this concept of label retention to examine this subpopulation of cancer cells in a murine model of breast cancer metastasis. We investigate the distribution of nonproliferative cancer cells within the primary tumor and the migration of these cells to distant lymph nodes.

Materials and Methods

Cell Culture and In Vitro *Experiments*

A green fluorescent protein (GFP) expressing transformant of the human breast cancer cell line MDA-MB-231 (231) was used. Cells were labeled with Flash Red fluorescent micron-sized superparamagnetic iron oxide (MPIO) particles (excitation: 660, emission: 690; Bangs Laboratories Inc, Fishers, IN). Briefly, 10^6 cells were plated onto T75 flasks with normal complete medium. After 24 hours, the medium was replaced with a labeling medium containing MPIO particles at a concentration of 0.049 mg Fe/ml and cells were incubated for another 24 hours before being harvested.

To determine how MPIO particles diluted with proliferation, the cells were harvested on days 1, 2, 4, 7, 10, and 14 after addition of the labeling medium (n = 3 flasks per time point). A cell sample was taken from each flask at all time points, centrifuged onto microscopy slides, and stained for iron with Perls' Prussian Blue (PPB). The number of iron-labeled cells and the total number of cells were counted in five different fields of view from each sample and the percentage of labeled cells was determined for each time point.

This experiment was repeated and analyzed using flow cytometry. We collected cell samples at days 1, 2, 4, 7, 10, and 14 (n = 3 flasks per time point). All analyses were performed using an LSR II flow cytometer (Becton Dickinson, Mississauga, Ontario). The fluorescence signal of the MPIO particles' Flash Red label was obtained by excitation with a 640-nm laser and detected using a 670/30 filter, and 2×10^5 events were acquired. The iron content of cells at each time point was assessed by examining the amount of fluorescence of the MPIO particles in each sample. A sample of unlabeled 231 cells was also collected for use as a control.

Animal Model

Unlabeled (n = 8) or MPIO-labeled (n = 8) GFP-positive 231 cells (5×10^5) were injected into the right thoracic mammary fat pad of female CB-17 severe combined immune deficiency (SCID; CB17/Icr-Prkdc^{scid}/IcrIcoCrl) mice aged 6 to 8 weeks (Charles River Laboratories, Wilmington, MA). Animals were imaged using MRI on days 0, 7, 14, 21, and 28 after the cell injection. Mice were sacrificed either after the appearance of signal loss in MR images of either the ipsilateral axillary or brachial lymph nodes (five of eight mice in labeled group) or on day 28 after all imaging had been completed.

MRI Methods

All imaging sessions were conducted using a 1.5-T CV/I MRI scanner (General Electric Medical Systems, Milwaukee, WI) along with a custom-built gradient coil insert (inner diameter = 17.5 cm, maximum gradient strength = 500 mT/m, and peak slew rate = 3000 T/m/s) and a custom-built solenoid mouse body radio-frequency coil (4 cm in length and 3 cm in diameter). All images were acquired with a three-dimensional balanced steady-state free precession (bSSFP) pulse sequence. The bSSFP sequence was chosen because it provides very high signal-to-noise ratio efficiency, allowing for high-resolution image acquisitions of the whole mouse body in reasonable scan times, and because it produces very good soft tissue contrast, related to T2/T1. The scan parameters for bSSFP were given as follows: repetition time = 6.7 milliseconds, echo time = 3.3 milliseconds, flip angle = 40°, bandwidth = ±31.25 kHz, matrix = 300 × 300, field of view = 6 cm, 0.2-mm slice thickness, 200-μm isotropic spatial resolution, four signal averages, four radio-frequency phase cycles, and scan time of 34 minutes.

Microscopy Methods

The left and right axillary and brachial lymph nodes and the primary tumors were removed from the animals at necropsy. The tissues were then placed in 3.75% formaldehyde in 0.1 M phosphate buffer overnight to fix the tissue. Some lymph nodes and tumors were then paraffin embedded for PPB staining and others were placed in a sucrose gradient over the next 3 days, followed by embedding in OCT compound for cryosectioning for fluorescence microscopy. Tissue samples were cut into 5-μm sections for paraffin-embedded samples and 16 μm for frozen samples. For fluorescence microscopy, frozen lymph node sections were thawed and stained with 4′,6-diamidino-2-phenylindole (DAPI) for cell nuclei. PPB staining was performed on both frozen and paraffin-embedded sections. All microscopy was performed on a Zeiss AXIO Imager (Carl Zeiss Canada Ltd, Toronto, Ontario). Fluorescence images were taken using GFP, Texas Red, and DAPI filters. Confocal fluorescence images were acquired on a Fluoview FV10i confocal microscope (Olympus Canada Inc, Richmond Hill, Ontario) using a 473-nm laser for GFP and a 635-nm laser for Cy5.5 excitation.

Image Analysis

The volume of the tumors and the left and right axillary and brachial lymph nodes were measured by manual segmentation using the OsiriX image analysis software [21]. The axillary and brachial lymph nodes

were chosen for analysis because these nodes are primarily responsible for draining the area of the mammary fat pad where the cells were injected. The OsiriX image analysis software [21] was used to make all measurements from the images acquired in this study. Each tumor or lymph node was segmented individually on every image slice to create a series of regions of interest. The volume was then calculated by using the region-of-interest volume calculation tool available within the software package.

Tumor maps that distinguished between low signal intensities generated from iron oxide particles (blue-colored zone), intermediate signal intensities associated with tumor parenchyma (green-colored zone), and high signal intensities related to fluid within the tumor (yellow-colored zone) were created. The image analysis program ImageJ [22] was used to generate the cutoff values for the low and high signal intensities.

Images of single PPB-stained sections were compared with composite images of six individual images of PPB-stained sections that were merged using the Adobe Photoshop Elements 8 software package (Adobe Systems Incorporated, San Jose, CA). Briefly, six images of consecutive PPB-stained tissue sections were overlaid and aligned. Areas of positive staining were outlined in each section and a new image layer was created from the outlined areas, colored blue, and made visible above one image of the PPB-stained tissue sections.

All statistical analyses were done using the GraphPad Prism software (GraphPad Software, Inc, La Jolla, CA). Data were analyzed using the repeated measures analysis of variance test, the Student's *t* test, and the nonparametric Mann-Whitney test. *P* values were considered significant if they were less than .05.

Results

In Vitro *Iron Dilution*

231 cells were labeled *in vitro* with MPIO particles and their iron content was assessed at days 1, 2, 4, 7, 10, and 14 after labeling by counting PPB+ cells in stained cell samples or by measuring the amount of red fluorescence associated with the MPIO using flow cytometry. Cell viability after labeling (day 1 time point) was 99.2 ± 0.6%. Figure 1 shows the PPB-stained cell samples along with the quantification of the percentage of PPB-positive–labeled cells detected at each time point. As the cells divided, the numbers of cells that contained iron particles decreased. At days 1 and 2 after labeling, 99.0 ± 0.3% and 86.0 ± 1.4% of cells were labeled. The number of labeled cells decreased to 43.1 ± 1.6% at day 4, 7.6 ± 1.6% at day 7, 1.0 ± 0.3% at day 10, and 0.8 ± 0.3% at day 14.

Similar results were observed when cells were analyzed using flow cytometry. Figure 2*A* shows the percentage of iron-labeled cells, based on the red fluorescence associated with MPIO, at each time point. At days 1 and 2 after labeling, 99.9 ± 0.1% and 97.0 ± 0.1% of cells were positive for the red fluorescent particles. The number of labeled cells decreased to 45.7 ± 1.4% at day 4, 9.5 ± 0.9% at day 7, 2.6 ± 0.9% at day 10, and 0.5 ± 0.1% at day 14. Figure 2*B* shows representative dot plots of the flow cytometry data collected for each time point. The plots display the fluorescence of the particles in the red channel on the *x*-axis and side scatter on the *y*-axis. Although the iron content diluted as cells proliferated, iron-labeled cells could still be detected at 14 days after labeling.

MRI of Primary Tumor

Images of iron-labeled tumors (Figure 3*A*) had large, obvious areas of signal loss within the developing mass. At day 14, developing tumors appeared with mainly low signal intensity throughout. At day 21, the MRI of tumors showed regions of low signal along with regions of mixed, heterogeneous signal intensities. Images acquired on day 28 show that as the tumors became larger the regions of signal loss persisted and more of the tumor mass appeared with intermediate/high signal intensities. The images of tumors that developed from unlabeled 231 cells (Figure 3*B*) had a different MRI appearance. These tumors had a homogeneous, intermediate signal intensity at day 14 and became more heterogeneous in signal as the tumors grew in size. However, regions of hypointensity, such as observed in images of the iron-labeled tumors, were not observed in unlabeled tumors.

Tumor color maps are shown together with the MRI to assist with visualization of the tumor borders and to highlight the three zones of signal intensities observed. Blue represents the regions of signal hypointensity (due to iron particles), yellow represents regions of hyperintense signal (most likely due to fluid/necrosis), and green represents

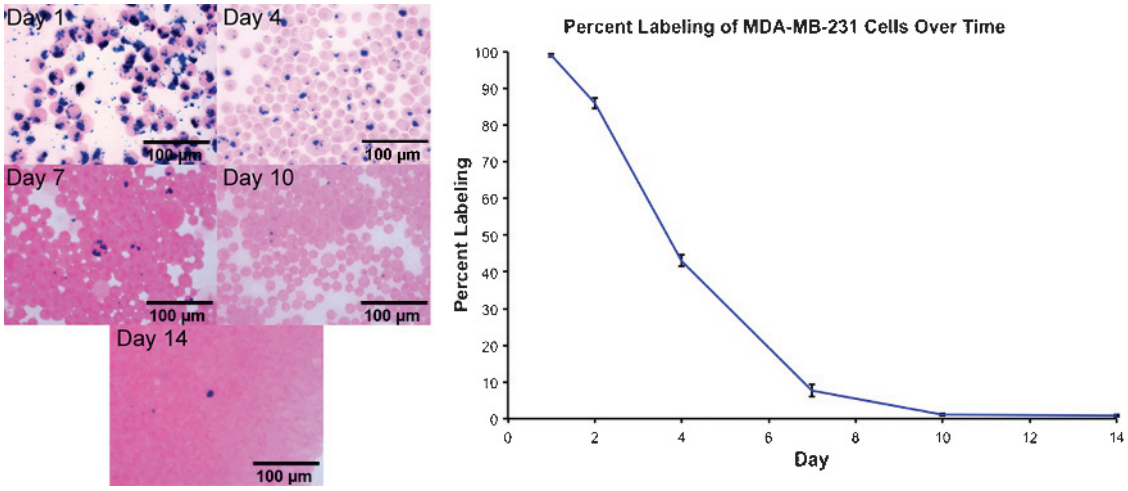

Figure 1. Stained cell samples of MPIO-labeled MDA-MB-231 cells at 1, 4, 7, 10, and 14 days after labeling. Graph of percentage of iron-labeled MDA-MB-231 cells over time.

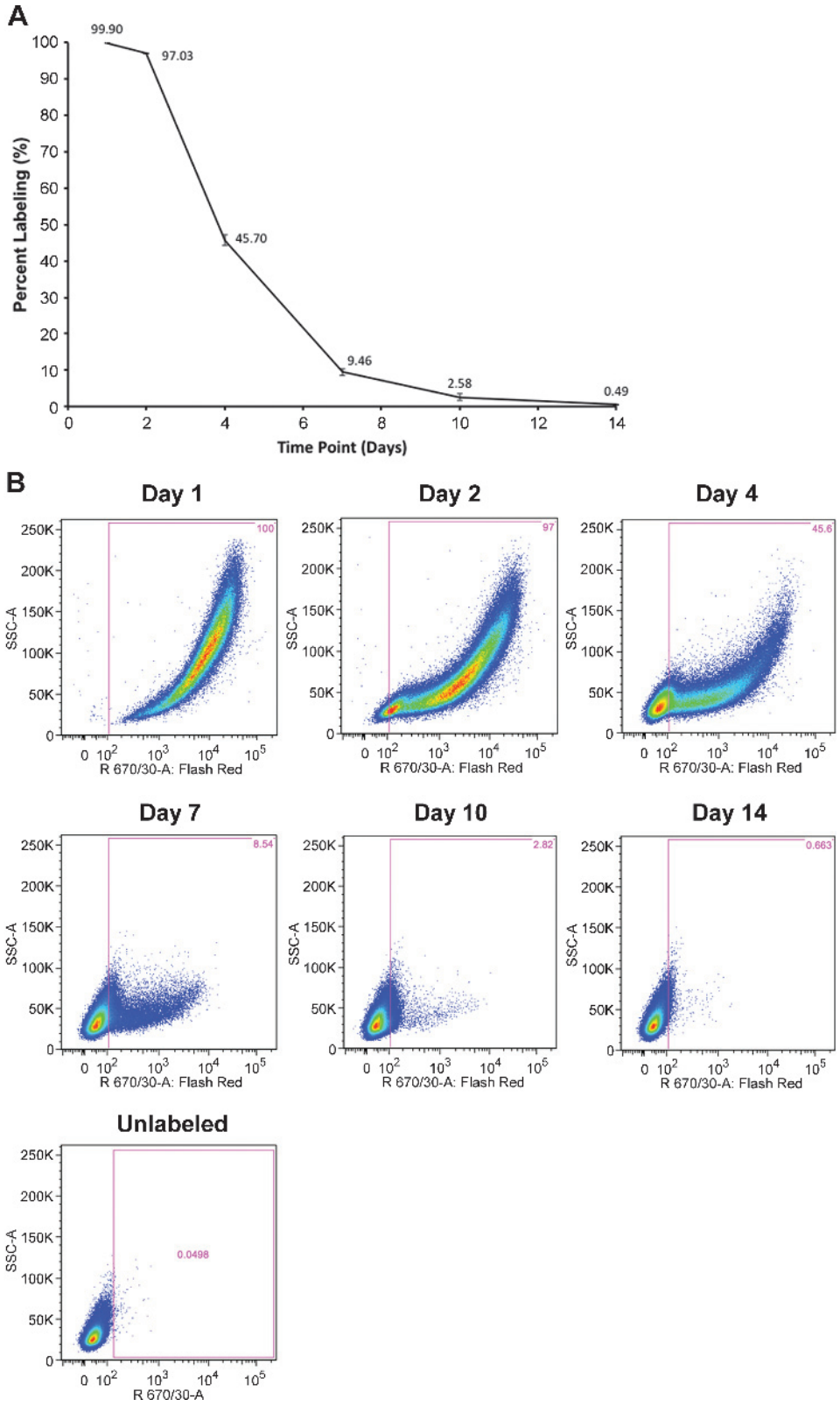

Figure 2. *In vitro* dilution of MPIO particles in MDA-MB-231 cells measured by flow cytometry. (A) Graph of percentage of iron-labeled MDA-MB-231 cells over time. (B) Plots of Flash Red fluorescence intensity (*x*-axis) *versus* side scatter (*y*-axis) at days 1, 2, 4, 7, 10, and 14 with gates shown for the labeled population (based on unlabeled control sample).

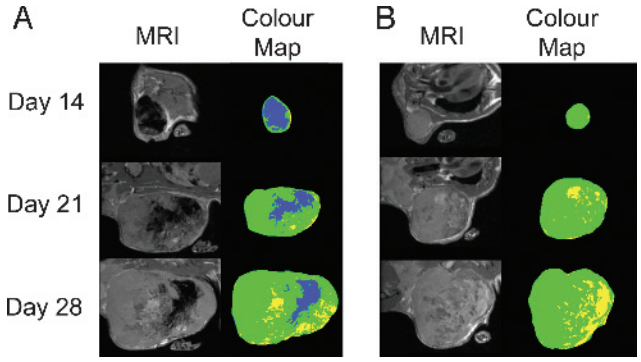

Figure 3. Appearance of labeled and unlabeled tumors over time and corresponding tumor color maps. (A) The MR image and color map, respectively, of a labeled tumor over time. (B) The MR image and color map, respectively, of an unlabeled tumor. For color maps, blue represents below low intensity cutoff (day 7, 255; day 14, 288; day 21, 301; day 28, 320), green represents between low intensity cutoff and high intensity cutoff (signal intensities of 700), and yellow represents above high intensity cutoff.

the intermediate signal intensities (the bulk of the tumor mass). There is a distinct difference in the color maps for labeled (Figure 3*A*) and unlabeled tumors (Figure 3*B*). The percentage of the total tumor volume within each of the three zones was measured for all tumors and is shown in Table 1. For iron-labeled tumors, 91.4% of the tumor volume was composed of the low signal intensity zone (blue in color map) at the first imaging time point (day 7) and this decreased to 4.6% at the last imaging time point (day 28). In comparison, 1% or less of the volume of unlabeled tumors fell within this zone at any time point. The percentage of the tumor volume within the low signal intensity zone was compared between labeled and unlabeled groups at each time point using a Mann-Whitney test. Significant differences were found at all times (day 7, $P = .004$; day 14, $P = .0007$; day 21, $P = .0095$; day 28, $P = .0238$). There was no significant difference in total tumor volume between the iron-labeled and unlabeled tumors at any imaging time point.

Histology of Primary Tumor

Tumors were sectioned and stained for iron with PPB. Figure 4 depicts a tumor generated from MPIO-labeled 231 cells at day 14 after injection. Figure 4, *A*, *D*, and *F*, shows a single 16-μm PPB-stained section of the tumor at increasing magnification. These sections show the presence of iron-labeled cells within the tumor. Figure 4, *B* and *E*, shows merged images of six consecutive PPB-stained sections showing the summed iron content of all six sections. The data are presented this way to illustrate the conundrum of comparing 16-μm stained tissue sections with 200-μm MRI slices. A total of 12 tissue sections like these would have to be merged perfectly for a true representation of the extent of iron-labeled cells contained in the image slice. Overall, all tumors contained iron-labeled cells distributed throughout the tumor mass.

Detection of Regions of Signal Loss in Lymph Nodes

Of particular interest was the observation of regions of signal loss in images of the draining lymph nodes, in six of eight mice that received MPIO-labeled 231 cells. Figure 5, *A* (arrow), *B*, and *C*, shows a representative image of an ipsilateral axillary lymph node at day 14 with a focal region of signal loss and the corresponding PPB-stained sections, respectively. The MRI and histology showed good correspondence. In this example, signal loss was observed on one side of the node and the most intense PPB staining was located in the same location. Fluorescence microscopy was used to validate the presence of MPIO+ cancer cells within nodes.

In Figure 6, *A* to *D*, an ipsilateral axillary node that showed a region of signal loss at day 28 was found to contain GFP+ cells and regions of red fluorescence that were co-localized, indicating the presence of iron-labeled cancer cells in the node. Confocal microscopy was also performed on some lymph nodes (Figure 7). Tissue sections were imaged with GFP and Cy5.5 fluorescence. Confocal image overlays of an ipsilateral axillary lymph node at 28 days after the 231 cell injection clearly show the presence of a number of GFP+ cells, which contain red fluorescent particles, located in the node. These data also indicate that the cancer cells have retained the MPIO label after migrating from the tumor to the node.

Fluorescence microscopy images of the lymph node sections also revealed that areas of green and red fluorescence did not always overlap. Occasionally, red fluorescent areas that correlated with DAPI staining for cell nuclei but not with areas of green fluorescence were found (data not shown). This suggests that the red fluorescent iron particles can be found in other cell types within the lymph node and may represent bystander cell uptake of iron associated with dead tumor cells.

Tables 2 and 3 summarize the analysis of axillary and brachial lymph nodes that were examined with both MRI and microscopy. The time point that each node was examined at is also included in these tables. Table 2 shows that five of six axillary lymph nodes were positive for signal loss in MR images and that the presence of iron-labeled cells was confirmed for all five nodes, with either PPB staining or fluorescence microscopy. One axillary node did not have signal loss within it (was MRI negative); however, fluorescence microscopy revealed cells in the node that were both GFP and red MPIO positive. The sensitivity of detection of signal loss by MRI due to iron-labeled cells in the axillary nodes was therefore 83%.

Table 3 shows that two of five brachial lymph nodes were positive for signal loss on MRI; iron-labeled cells were detected by PPB

Table 1. Tumor Volume and Percentage of Tumor Volume in Tumor Color Map Zones.

	Percentage in Blue Zone		Percentage in Green Zone		Percentage in Yellow Zone		Tumor Volume (mm^3)	
	Labeled Tumors	Unlabeled Tumors	Labeled Tumors	Unlabeled Tumors	Labeled Tumors	Unlabeled Tumors	Labeled Tumors	Unlabeled Tumors
Day 7	91.4 ± 15.0	0.5 ± 0.4	7.8 ± 13.1	98.2 ± 1.0	0.8 ± 1.9	1.3 ± 0.9	16.3 ± 7.3	10.2 ± 4.7
Day 14	81.4 ± 6.8	0.4 ± 0.5	17.5 ± 6.1	98.5 ± 0.6	1.2 ± 1.1	1.0 ± 0.8	169.9 ± 81.9	158.5 ± 90.4
Day 21	12.1 ± 6.1	0.1 ± 0.05	85.2 ± 6.6	88.7 ± 7.0	2.7 ± 0.8	11.4 ± 7.0	839.9 ± 496.2	1003.7 ± 443.5
Day 28	3.4 ± 2.4	0.1 ± 0.02	87.7 ± 7.5	85.2 ± 5.1	9.0 ± 5.1	14.8 ± 5.1	1994.5 ± 661.1	2574.7 ± 891.0

The blue zone is below low intensity cutoff (signal intensity of 255), the green zone is between low intensity cutoff and high intensity cutoff (signal intensity of 700), and the yellow zone is above high intensity cutoff.

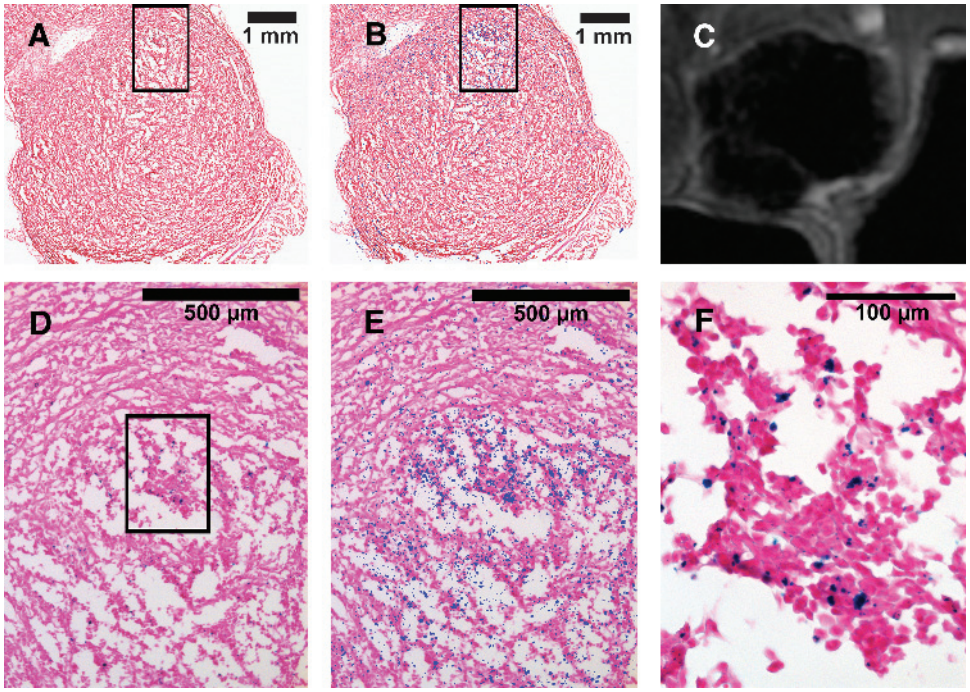

Figure 4. PPB-stained section of labeled tumor at day 14. (A) PPB-stained section of tumor lobe. (B) PPB-stained section showing the iron content from six consecutive sections (blue areas). (C) MR image of tumor. (D) PPB-stained section of tumor from area outlined by box in A. (E) PPB-stained section showing the iron content from six consecutive sections (blue areas), from area outlined by box in B. (F) PPB-stained section of tumor from area outlined by box in D.

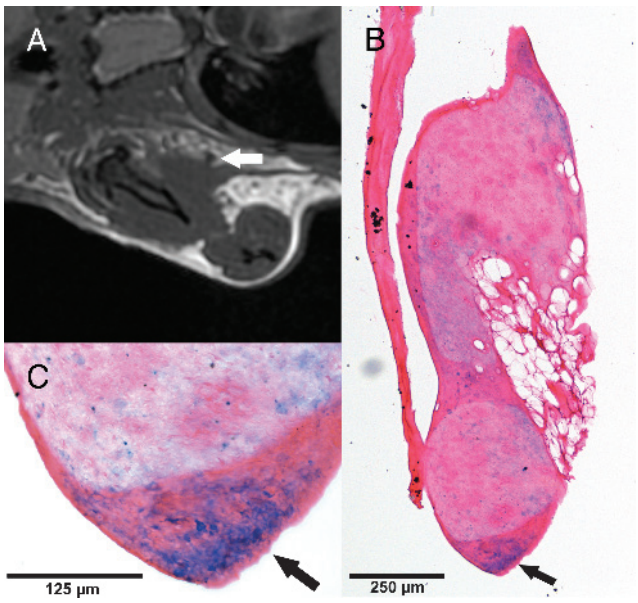

Figure 5. MRI and iron staining of an ipsilateral axillary lymph node 14 days after iron-labeled breast cancer cells were implanted into the thoracic mammary fat pad in CB17 SCID mice. (A) Cropped bSSFP image of thorax region of mouse reveals a region of signal loss in the ipsilateral axillary node (arrow). (B) Section of lymph node stained with PPB for iron detection at ×10 magnification shows iron-positive cells in the area of the node corresponding to the signal loss in the MR image (arrow). (C) Iron-positive area of the node at ×40 magnification, where strong staining can be seen (arrow) suggesting that cancer cells have retained iron particles after migrating to the node.

staining in both of these nodes. For three brachial lymph nodes, no signal loss was detected by MRI even though the fluorescence microscopy for all three of these nodes showed cells that were both GFP and red MPIO positive. The sensitivity of detection of signal loss by MRI due to iron-labeled cells in the brachial lymph node was only 40%.

Discussion

The goal of this study was to investigate the potential for tracking metastatic cancer cells using iron oxide nanoparticles and MRI. We have demonstrated that the retention of iron particles in some cancer cells allows for their long-term tracking *in vivo*. Previously, we studied the fate of iron-labeled cancer cells in a model of breast cancer metastasis to the brain [14] and in a model of melanoma metastasis in the liver [15]. In those models, cancer cells were delivered to the organ of interest (brain or liver) by systemic injection (intracardiac left ventricle or intrahepatic vein) to mimic the hematogenous spread of metastatic cancer cells. In the current study, we have used an orthotopic model of breast cancer and have examined the draining lymph nodes for metastasis.

Cell tracking with MRI and magnetic nanoparticles has not been widely applied to study cancer cells because the iron label is diluted during cell division. Since the detection of iron-labeled cells by MRI relies on the total iron content, this means that eventually the cancer cells will not contain enough iron to be detected as signal voids in MR images. Early *in vitro* studies by Arbab et al. showed that mesenchymal stem cells, which are slowly dividing cells in culture, retained SPIO particles for up to 7 weeks after cell labeling, whereas iron-labeled cancer cells (HeLa) lost their iron label by 2 to 3 weeks after cell labeling [23]. We have previously reported the dilution of SPIO in fast

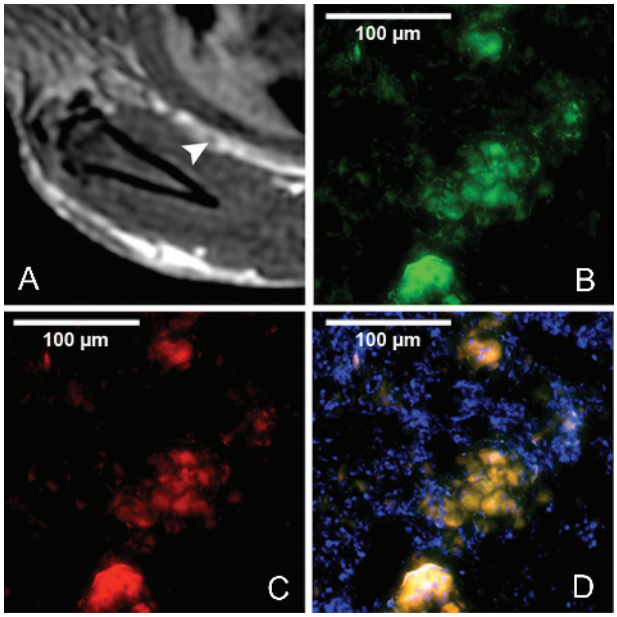

Figure 6. MRI and fluorescence microscopy of a representative SCID mouse ipsilateral axillary lymph node 28 days after tumor cell implantation. CB17 SCID mice were injected with GFP-positive MDA-MB-231 cells labeled with red fluorescent iron oxide particles. (A) Cropped bSSFP MRI image of the ipsilateral axillary lymph node shows a region of signal loss within the node (arrowhead). (B) GFP-positive cancer cells found within node correspond with (C) red fluorescent MPIO particles. (D) Overlay of GFP fluorescent cells, red fluorescent MPIO, and DAPI stain for cell nuclei. Cells that are positive for both GFP and contain red fluorescent particles can be found within the node, confirming the presence of iron-labeled cancer cells.

growing mouse melanoma (B16F10) cancer cells to below MR detectable levels in only 4 to 5 days after cell labeling [24]. In the current study, both the analysis of PPB-stained cells in stained cell samples and the flow cytometric analysis showed that *in vitro* by day 4 after cell labeling the number of MPIO-labeled 231 cells was under 50% and that this declined to less than 5% at day 10 after labeling. Still, at 14 days (~14 cell divisions) after labeling, a very small proportion of the cancer cells retained the iron label. This finding is in agreement

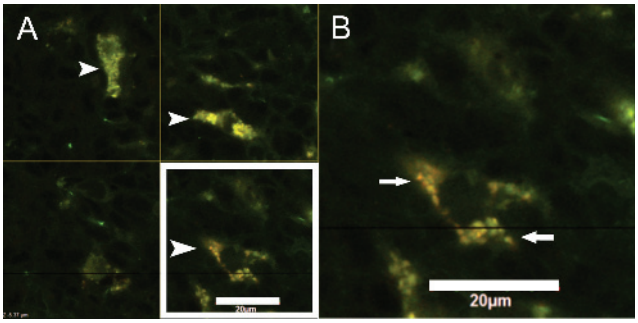

Figure 7. Confocal microscopy image of MPIO-labeled MDA-MB-231 cells in an ipsilateral axillary lymph node 28 days after tumor cell implantation. (A) Image at ×60 magnification. Area in white box has been enlarged (B) to show the localization of MPIO particles (red) in the cells (green).

Table 2. Analysis of Axillary Lymph Nodes Examined with Both MRI and Either PPB Staining or Fluorescence Microscopy.

Axillary Lymph Node	Signal Loss in MR Images	Positive in Microscopy (Positive PPB Staining or GFP and Red MPIO-Positive Cells)	Time Point Removed
1	Yes	Yes, PPB	Day 14
2	Yes	Yes, PPB	Day 14
3	Yes	Yes, FL	Day 14
4	Yes	Yes, FL	Day 21
5	No	Yes, FL	Day 14
6	Yes	Yes, FL	Day 28

FL indicates fluorescence microscopy.

with a study by Magnitsky et al. who detected a small population of MPIO-retaining human melanoma cells (~1%) at day 20 after cell labeling (~17 cell divisions). They also used demonstrated a correlation between iron-retaining cells and expression of JARID1B, a biologic marker of slow cycling cells [16].

Our *in vivo* MRI data also show that not all cancer cells lose the iron label over time, indicating that not all cancer cells undergo extensive proliferation. This is perhaps expected since solid tumors are known to have pronounced heterogeneity, with different subpopulations of cancer cells (and normal stromal cells) co-existing. The list of characteristics by which these subpopulations differ is extensive but includes cellular morphology, receptors, enzymes, growth rates, and gene expression to name a few [25]. Marked differences in the proliferation behavior of tumor cells within a single cancer are typical [25]. Some cells are nonproliferative and others are cycling, but this can occur at various rates, and at any given time, cycling cells within the tumor will be at different stages of the cell cycle.

MRI of the primary mammary fat pad tumors showed that the iron-labeled cells (blue zone) encompass the whole tumor in the first 2 weeks and then, as the tumor volume increases, make up less of the tumor mass and appear to remain located together in one region of the tumor. Because sister cells have been shown to remain contiguous in solid tumors, sublines tend to be localized regionally or zoned [26–28]. Therefore, the zone of iron-retaining cells within these tumors may reflect the presence of a specific subpopulation.

The ability to detect iron-labeled 231 cells in the ipsilateral axillary and brachial lymph nodes after implantation of these cells in the mammary fat pad is intriguing. Because we rarely observed GFP+ cancer cells in the nodes that were not also red fluorescent, our data suggest that there may be a relationship between the iron-retaining cell population and an invasive or metastatic phenotype. This is the first paper to demonstrate the migration of iron-labeled cancer cells from a primary tumor using MRI. The sensitivity of detecting signal loss by

Table 3. Analysis of Brachial Lymph Nodes Examined with Both MRI and Either PPB Staining or Fluorescence Microscopy.

Brachial Lymph Node	Signal Loss in MR Images	Positive in Microscopy (Positive PPB Staining or GFP and Red MPIO-Positive Cells)	Time Point Removed
1	Yes	Yes, PPB	Day 14
2	Yes	Yes, PPB	Day 14
3	No	Yes, FL	Day 14
4	No	Yes, FL	Day 21
5	No	Yes, FL	Day 28

FL indicates fluorescence microscopy.

MRI due to the presence of iron-labeled cancer cells was found to be 83% for the axillary node and 40% for the brachial node. This is likely because the axillary nodes in the mouse are easier to visualize in the MR images than the brachial nodes because the axillary node sits in a more prominent fat pad that generates very good image contrast in bSSFP images (fat is bright; node tissue is intermediate).

Our data suggest that nonproliferative, or slowly cycling, cancer cells can be detected by *in vivo* MRI. Nonproliferative cancer cells, sometimes referred to as dormant cells, are believed to contribute to tumor recurrence. Clinical dormancy is reflected by relapses at distant sites after the original primary cancer diagnosis. In some tumors, for example, breast cancer, melanoma, and renal cancer, these recurrences are common and can occur many years after diagnosis [29]. Dormant cancer cells also present a substantial therapeutic problem; because they are quiescent, they are nonresponsive to current therapies that target proliferating cells [16–18]. Discerning the mechanisms that either maintain prolonged cellular dormancy or activate dormant tumor cells to a proliferative state has been a recognized goal of scientists worldwide. Still, relatively little is known about dormant cancer cells and studying these cells is challenging since, at the present time, there are no suitable *in vivo* assays. It is exciting to consider that advanced *in vivo* cellular imaging techniques, as described in this paper, may be used to study the fate of distinct subpopulations of metastatic breast cancer cells within the whole tumor in the intact mouse body.

Acknowledgments

We thank Francisco Martinez and Andrew Alejski for assistance with MRI hardware, Kristin Chadwick and Gabrielle Siegers for assistance with flow cytometry, and Amanda Hamilton and Emeline Ribot for assistance with editing and useful discussion.

References

[1] Modo M, Hoehn M, and Bulte JWM (2005). Cellular MR imaging. *Mol Imaging* **4**, 143–164.

[2] Yang K, Xiang P, Zhang C, Zou L, Wou X, Gao Y, Kang Z, He K, Liu J, and Peng C (2011). Magnetic resonance evaluation of transplanted mesenchymal stem cells after myocardial infarction in swine. *Can J Cardiol* **27**, 818–825.

[3] Yao Y, Li Y, Ma G, Liu N, Ju S, Jin J, Chen Z, Shen C, and Teng G (2011). *In vivo* magnetic resonance imaging of injected endothelial progenitor cells after myocardial infarction in rats. *Mol Imaging Biol* **13**, 303–313.

[4] Daadi MM, Li Z, Arac A, Grueter BA, Sofilos M, Malenka RC, Wu JC, and Steinberg GK (2009). Molecular and magnetic resonance imaging of human embryonic stem cell-derived neural stem cell grafts in ischemic rat brain. *Mol Ther* **17**, 1282–1291.

[5] Jendelová P, Herynek V, Urdzíková L, Glogarová K, Kroupová J, Andersson B, Bryja V, Burian M, Hájek M, and Sykova E (2004). Magnetic resonance tracking of transplanted bone marrow and embryonic stem cells labeled by iron oxide nanoparticles in rat brain and spinal cord. *J Neurosci Res* **76**, 232–243.

[6] Gonzalez-Lara LE, Xu X, Hofstetrova K, Pniak A, Chen Y, McFadden CD, Martinez-Santiesteban FM, Rutt BK, Brown A, and Foster PJ (2011). The use of cellular magnetic resonance imaging to track the fate of iron-labeled multipotent stromal cells after direct transplantation in a mouse model of spinal cord injury. *Mol Imaging Biol* **13**, 702–711.

[7] Kim H, Walczak P, Muja N, Campanelli JT, and Bulte JWM (2012). ICV-transplanted human glial precursor cells are short-lived yet exert immunomodulatory effects in mice with EAE. *Glia* **60**, 1117–1129.

[8] Dekaban GA, Snir J, Shrum B, de Chickera S, Willert CJ, Merril M, Said EA, Sekaly R-P, Foster PJ, and O'Connell PJ (2009). Semiquantitation of mouse dendritic cell migration *in vivo* using cellular MRI. *J Immunother* **32**, 240–251.

[9] Zhang X, de Chickera SN, Willert C, Economopoulos V, Noad J, Rohani R, Wang AY, Levings MK, Scheild E, Foley R, et al. (2011). Cellular magnetic resonance imaging of monocyte-derived dendritic cell migration from healthy donors and cancer patients as assessed in a scid mouse model. *Cytotherapy* **13**, 1234–1248.

[10] de Vries IJM, Lesterhuis WJ, Barentsz JO, Verdijk P, Han van Krieken J, Boerman OC, Oyen WJG, Bonenkamp JJ, Boezeman JB, Adema GJ, et al. (2005). Magnetic resonance tracking of dendritic cells in melanoma patients for monitoring of cellular therapy. *Nat Biotechnol* **23**, 1407–1413.

[11] Heyn C, Ronald JA, MacKenzie LT, MacDonald IC, Chambers AF, Rutt BK, and Foster PJ (2006). *In vivo* magnetic resonance imaging of single cells in mouse brain with optical validation. *Magn Reson Med* **55**, 23–29.

[12] Shapiro EM, Sharer K, Skrtic S, and Koretsky AP (2006). *In vivo* detection of single cells by MRI. *Magn Reson Med* **55**, 242–249.

[13] Walczak P, Kedziorek DA, Gilad AA, Barnett BP, and Bulte JWM (2007). Applicability and limitations of MR tracking of neural stem cells with asymmetric cell division and rapid turnover: the case of the shiverer dysmyelinated mouse brain. *Magn Reson Med* **58**, 261–269.

[14] Heyn C, Ronald JA, Ramadan SS, Snir JA, Barry AM, MacKenzie LT, Mikulis DJ, Palmieri D, Bronder JL, Steeg PS, et al. (2006). *In vivo* MRI of cancer cell fate at the single-cell level in a mouse model of breast cancer metastasis to the brain. *Magn Reson Med* **56**, 1001–1010.

[15] Townson JL, Ramadan SS, Simedria C, Rutt BK, MacDonald IC, Foster PJ, and Chambers AF (2009). Three-dimensional imaging and quantification of both solitary cells and metastases in whole mouse liver by magnetic resonance imaging. *Cancer Res* **69**, 8326–8331.

[16] Magnitsky S, Roesch A, Herlyn M, and Glickson JD (2011). *In vivo* and *ex vivo* MR imaging of slowly cycling melanoma cells. *Magn Reson Med* **66**, 1362–1373.

[17] Naumov GN, MacDonald IC, Weinmeister PM, Kerkvliet N, Nadkarni KV, Wilson SM, Morris VL, Groom AC, and Chambers AF (2002). Persistence of solitary mammary carcinoma cells in a secondary site: a possible contributor to dormancy. *Cancer Res* **62**, 2162–2168.

[18] Luzzi KJ, MacDonald IC, Schmidt EE, Kerkvliet N, Morris VL, Chambers AF, and Groom AC (1998). Multistep nature of metastatic inefficiency: dormancy of solitary cells after successful extravasation and limited survival of early micrometastases. *Am J Pathol* **153**, 865–873.

[19] Cameron MD, Schmidt EE, Kerkvliet N, Nadkarni KV, Morris VL, Groom AC, Chambers AF, and MacDonald IC (2000). Temporal progression of metastasis in lung: cell survival, dormancy, and location dependence of metastatic inefficiency. *Cancer Res* **60**, 2541–2546.

[20] Goss PE and Chambers AF (2010). Does tumour dormancy offer a therapeutic target? *Nat Rev Cancer* **10**, 871–877.

[21] Rosset A, Spadola L, and Ratib O (2004). OsiriX: an open-source software for navigating in multidimensional DICOM images. *J Digit Imaging* **17**, 205–216.

[22] Abràmoff MD, Magalhães P, and Ram S (2004). Image processing with ImageJ. *Biophotonics Int* **11**, 36–42.

[23] Arbab AS, Bashaw LA, Miller BR, Jordan EK, Lewis BK, Kalish H, and Frank JA (2003). Characterization of biophysical and metabolic properties of cells labeled with superparamagnetic iron oxide nanoparticles and transfection agent for cellular MR imaging. *Radiology* **229**, 838–846.

[24] Foster PJ, Dunn EA, Karl KE, Snir JA, Nycz CM, Harvey AJ, and Pettis RJ (2008). Cellular magnetic resonance imaging: *in vivo* imaging of melanoma cells in lymph nodes of mice. *Neoplasia* **10**, 207–216.

[25] Heppner GH (1984). Tumor heterogeneity. *Cancer Res* **44**, 2259–2265.

[26] Fidler IJ and Hart IR (1981). Biological and experimental consequences of the zonal composition of solid tumors. *Cancer Res* **41**, 3266–3267.

[27] Hakansson L and Trope C (1974). On the presence within tumours of clones that differ in sensitivity to cytostatic drugs. *Acta Pathol Microbiol Scand A* **82**, 35–40.

[28] Prehn RT (1970). Analysis of antigenic heterogeneity within individual 3-methylcholanthrene-induced mouse sarcomas. *J Natl Cancer Inst* **45**, 1039–1045.

[29] Uhr JW and Pantel K (2011). Controversies in clinical cancer dormancy. *Proc Natl Acad Sci USA* **108**, 12396–12400.